Electronic Supporting Information (ESI) for:

Efficient triplet exciton phosphorescence quenching from a rhenium monolayer on silicon

William H. Banks[a,d], Michael P. Coogan[a], Tomas Markvart[b,c] and Lefteris Danos[a]*

[a]*Department of Chemistry, Energy Lancaster, Lancaster University, Lancaster, LA1 4YB, UK*

[b]*Solar Energy Laboratory, Faculty of Engineering and the Environment, University of Southampton, Southampton, SO17 1BJ, UK.*

[c]*Centre for Advanced Photovoltaics, Czech Technical University in Prague, Technická 2, 166 27 Prague 6, Czech Republic.*

[d]Current address: Cancer Research UK Manchester Institute, The University of Manchester, Wilmslow Road, Manchester M20 4BX, UK.

Experimental Details

1. Synthesis of rhenium tricarbonyl complex

ReC16 was prepared according to the literature precedent[1] (Fig. S1). Briefly, rhenium pentacarbonyl chloride was reacted with 2,2'-bipyridine to give *fac*-rhenium-2,2'-bipyridinetricarbonyl chloride, which was converted to the activated acetonitrile adduct, *fac*-rhenium-2,2'-bipyridinetricarbonylacetonitrile tetrafluoroborate, by halide abstraction with silver tetrafluoroborate. Reaction of *fac*-rhenium-2,2'-bipyridinetricarbonylacetonitrile tetrafluoroborate with pyridine-3-methyleneoxystearate in THF gave *fac*-rhenium-2,2'-bipyridinetricarbonylpyridinemethylene-3-oxystearate tetrafluoroborate, as previously described.

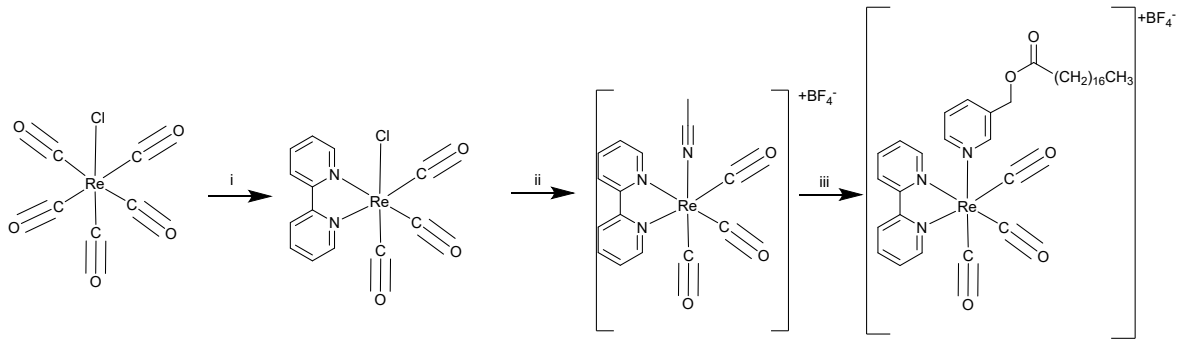

i) 2,2'bipyridine, PhMe, reflux 1h.
ii) $AgBF_4$, MeCN, reflux 1h.
iii) $PyCH_2O_2C(CH_2)_{16}CH_3$, THF, 50 C, 16h

Fig. S1 Reaction scheme for the synthesis of rhenium tricarbonyl complex ReC16.

2. Preparation of Langmuir-Blodgett (LB) films

Substrates of fused silica microscope slides (UQG Optics) and single crystal (111) silicon wafers (Pi-KEM) were first washed in a warm solution of Decon 90 detergent, using abrasion to clean the surfaces. The slides were then sequentially sonicated in Decon 90 and rinsed with deionised water (>18.0 MOhm.cm) and ethanol. Slides were dried and exposed to UV light in a UV Ozone system (Novascan, PSD Pro) at 60 ^{o}C for 15 minutes on each side, followed by exposure to piranha solution (3 parts H_2SO_4 to one-part H_2O_2) for at least 30 min. The samples were exposed to propanol vapours to dry the surface and with a final stream of nitrogen to remove any dust. Once the slides or silicon substrates had been cleaned, they were then exposed to hexamethyldisilazane vapours (HMDS) overnight in a lidded glass staining jar to give good hydrophobic adhesion to the surface.

A Langmuir-Blodgett (LB) trough (Nima Technology, UK) equipped with two dipping wells and barriers was used for all monolayer and multilayer deposition. An ultrapure water system (Arium pro UV, Sartorius) was used with a resistivity >18 MOhm cm and a pH between 6-7. Chloroform solutions of ReC16 or stearic acid (SA) with approximately 1mg/ml concertation were deposited in 30-50 µl aliquots onto the surface of water in the trough depending on the amount of material needed and left for 15 minutes to allow the solvent to evaporate. The pressure area isotherms for ReC16 were compressed ten times to improve packing in the ReC16 monolayer and to enable any residual solvent to evaporate. Langmuir monolayers were compressed (barrier speed = 50 cm^2/min) up to a pressure of 30 mN/m to prevent film damage (Fig. S2a).

Three compressions were performed before any deposition to allow the film to anneal. All monolayers (ReC16 and SA) were deposited at a constant pressure of 28 mN/m. The fused silica substrates were pre-coated with 6 layers of SA. After a single-layer deposition of ReC16 on the six layers of SA the layer was then capped with a further two layers of SA. Similarly, all ReC16 monolayers deposited on silicon substrates precoated with SA (to vary the distance) or silicon oxide substrates were all finally capped with two or three layers of SA. A direct hydrophilic or hydrophobic ReC16 layer was deposited on silicon substrates for distances 2−5 nm. A schematic of the sample structure is shown in Fig. S2b. A molecular model of ReC16 and the Re moiety is shown in Fig. S3.

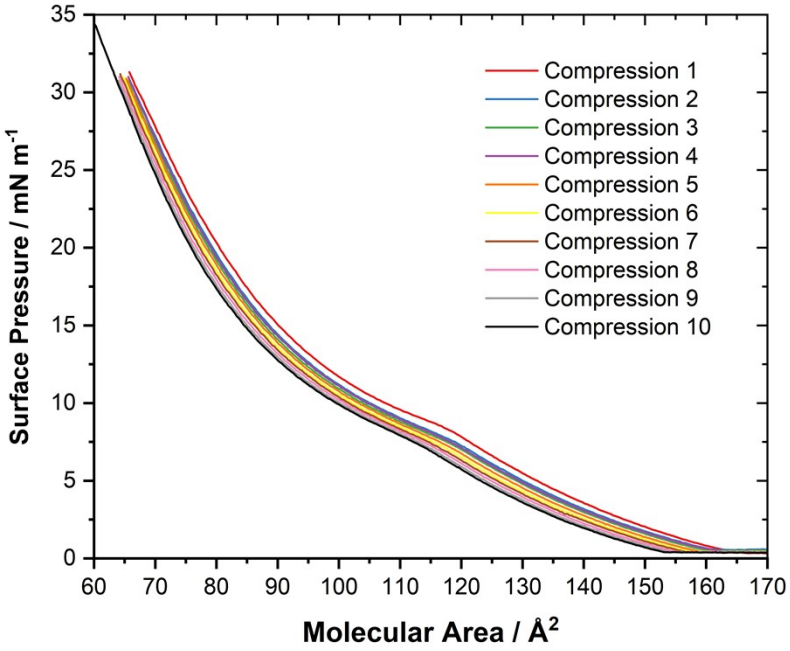

(a)

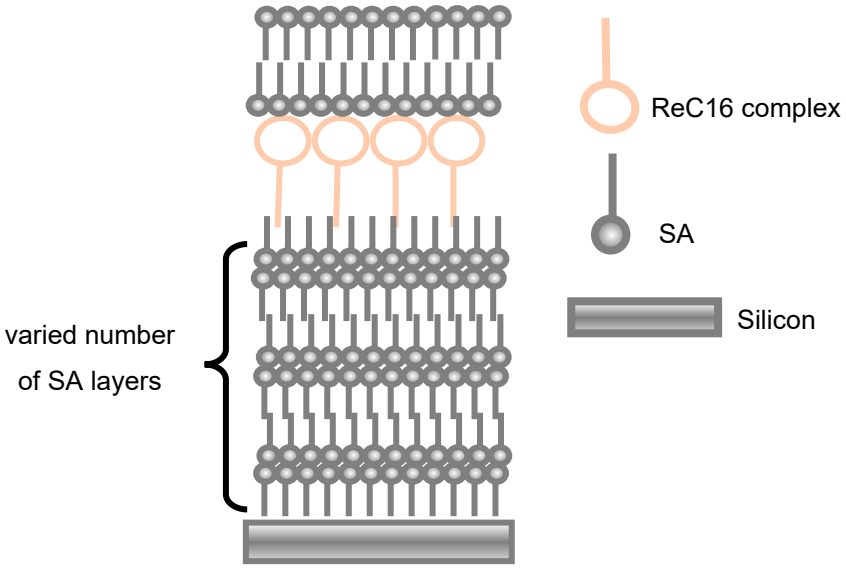

(b)

Fig. S2. (a) ReC16 isotherms on the surface of ultra-pure water over the course of ten compressions. (b) Schematic of the structure of the monolayer deposited on silicon substrates. The spacer stearic acid (SA) can be varied giving multiples of approximately 2.2 nm per monolayer from the surface of silicon.

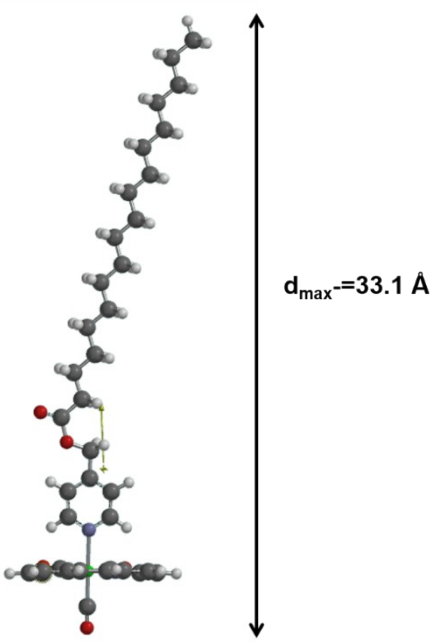

(a)

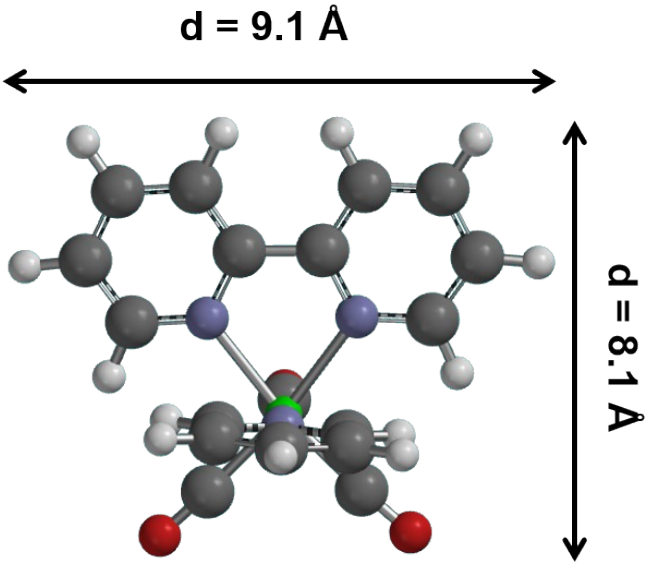

(b)

Fig. S3 Molecular model for (a) ReC16 and (b) Re moiety optimised in B3LYP/6-31G*.

3. Absorption spectra measurements

All absorption spectra were recorded in a UV-Vis absorption spectrometer (Cary 60, Agilent) in the spectral range 250−600 nm. Reference spectra were obtained using matching cuvettes (Starna Scientific Ltd, UK) for all solution measurements and UV fused silica microscope slides (UQG Optics) for all LB film measurements. Typical solution ($CHCl_3$) absorption spectra of ReC16 and from a ten-layer ReC16 film deposited on fused silica substrate are shown in Fig. S4. The spectra do not show any appreciable shift between the solution and the LB absorption.

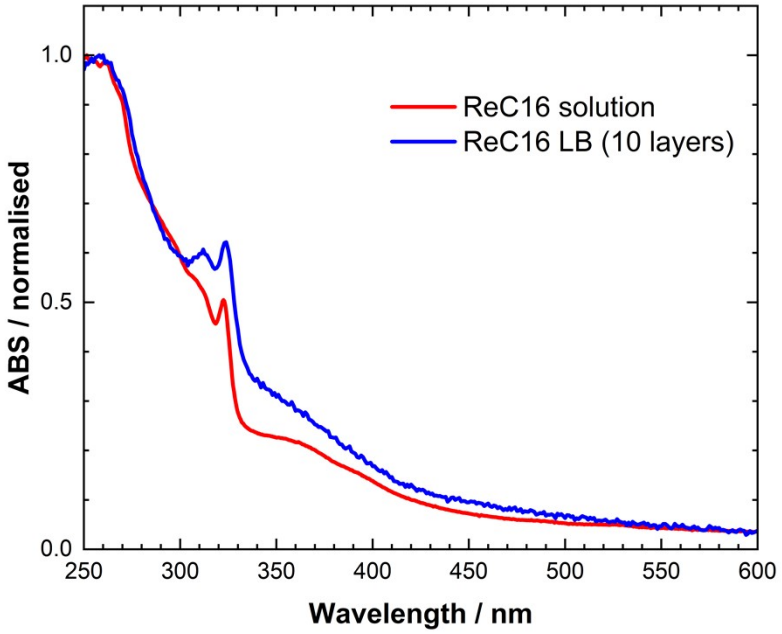

Fig S4 Normalised absorption spectrum of ReC16 in solution ($CHCl_3$) (red) and of a ten-layer ReC16 film (blue) deposited on a precoated fused silica substrate with six layers of SA and a further two layers of SA as a capping multilayer (see Fig. S2b).

4. Emission spectra measurements

A time-resolved fluorescence spectrometer (FluoTime 300, PicoQuant) was used to record all emission spectra. Samples were excited with a 405 nm (LDH-P-C-405, PicoQuant) or a 375 nm (LDH-P-C-375, PicoQuant) pulsed diode laser operated at 80 MHz. The emission spectrum was detected at right angle to the excitation beam with a Peltier cooled photomultiplier (PMA-C 192-M, PicoQuant) in the spectral range 450-700 nm and with a bandwidth of 5 nm. A 430 nm band edge filter (Semrock) was used to block unwanted laser scattering. Signals were digitised with a Time Harp 260 PCI card (PicoQuant) operated in steady-state detection mode. Examples of a typical ReC16 solution ($CHCl_3$) emission spectrum and that from a ReC16 monolayer deposited on fused silica substrate are shown in Fig S5. A blue shift is observed for the emission spectrum of the monolayer due to the low polarity of the lipophilic layers.

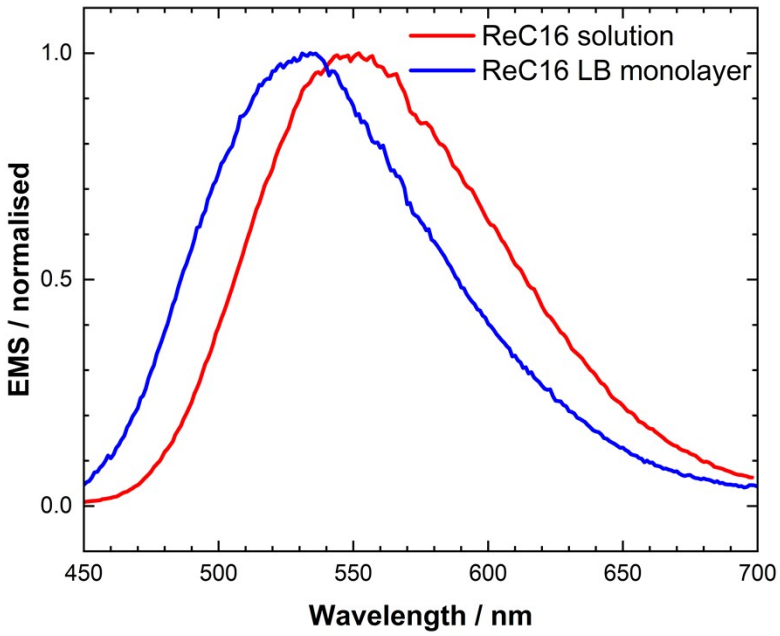

Fig. S5 Normalized emission spectrum of ReC16 in solution ($CHCl_3$) (red) with a λmax at 550 nm and normalized emission spectrum ReC16 monolayer (blue) with a λmax at 535 nm deposited on a pre-coated with six layers of SA fused silica substrate and a further two layers of SA as a capping multilayer (see Fig. S2b).

5. Phosphorescence lifetime decay measurements

Phosphorescence decay measurements were carried out using time-correlated single photon counting (TCSPC) on a FluoTime 300 (PicoQuant GmbH) system fitted with a 405 nm (LDH-P-C-405, PicoQuant) or a 375 nm (LDH-P-C-375, PicoQuant) pulsed diode laser with a variable repetition frequency range from 10-80 MHz. The setup is equipped with a Time Harp 260 PCI card (PicoQuant) operated in the long-range time mode and a Hamamatsu photomultiplier (PMA-C 192-M) with a spectral range from 300 nm to 900 nm. Phosphorescence signal sensitivity was improved by employing bursts of multiple pulses (100 pulses) which enabled high signal recovery from the long ReC16 phosphorescence lifetimes. Sample emission was collected at right angles to the excitation laser beam at 550 nm with a spectral bandwidth of 10 nm. All phosphorescence decay curves were analysed using the FluoFit software (PicoQuant GmbH) based on a single exponential decay model for solution measurements and a two or three-exponential model for the LB monolayer decay measurements. Pump, freeze and thaw experiments were also carried out to exclude oxygen from solutions.[2] The quality of the fits was assessed by the value of the reduced χ^2 value, and a visual inspection of the distribution of the weighted residuals and their autocorrelation function.[3] Examples of phosphorescence decay curves from ReC16 in solution and in a monolayer are shown in Fig. S6.

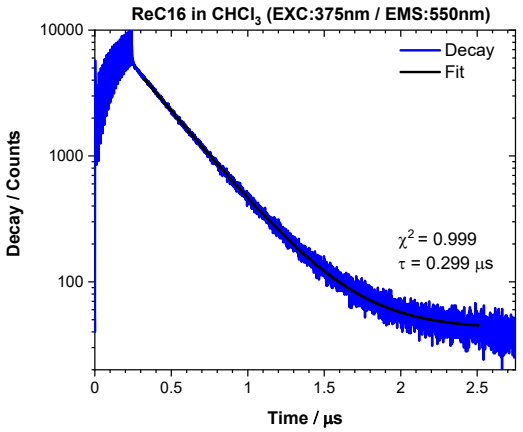

(a)

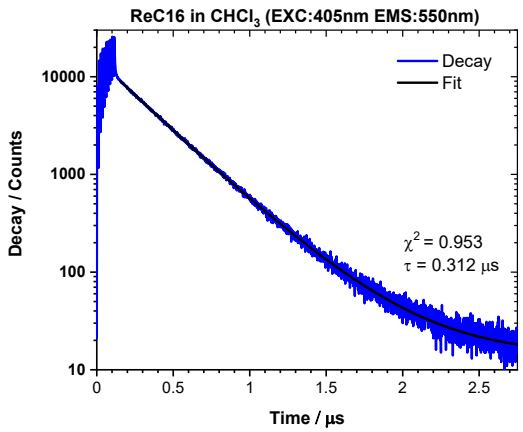

(b)

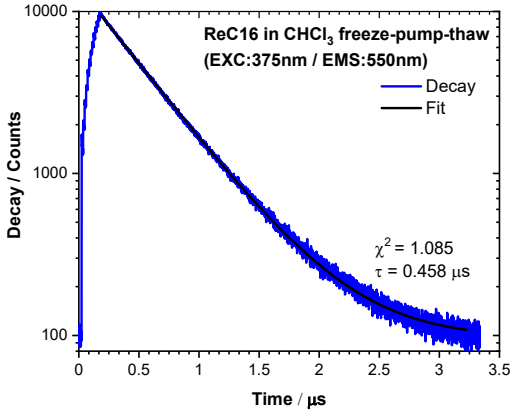

(c)

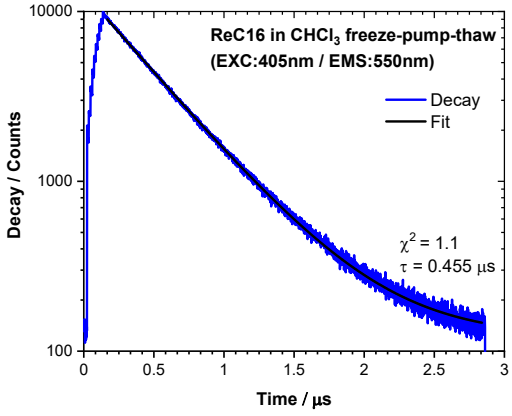

(d)

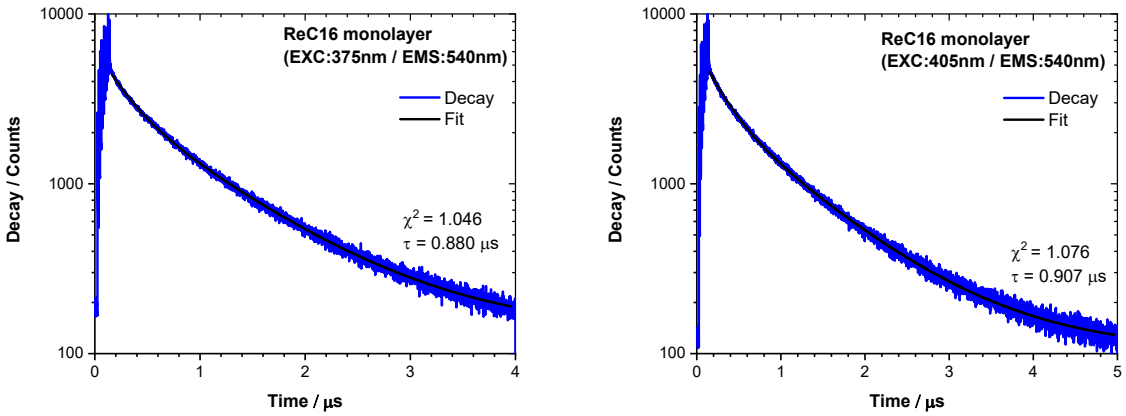

(e) (f)

Fig. S6 Decay curves from ReC16 in solution ($CHCl_3$) with a) 375 nm and b) 405 nm excitation wavelength. Pump freeze and thaw decay measurements for c) 375 nm and d) 405 nm excitation wavelength. Decay measurements from a ReC16 monolayer deposited on fused silica for e) 375 nm and f) 405 nm excitation wavelength.

6. Phosphorescence Lifetime Imaging Microscopy (PLIM)

Phosphorescence lifetime imaging microscopy measurements were performed on the ReC16 monolayers on fused silica and single crystal silicon substrates with an inverse fluorescence lifetime microscope (MT200, PicoQuant). The body of the microscope consisted of a modified Olympus IX73 equipped with a 100 × air lens objective with N>A. of 0.90 (MPlanFL N, Olympus). The MT200 system was configured with a scanning objective using a piezo XY stage (PI-721.CDQ) where the objective is moved instead of the sample. The samples were excited using a 405 nm pulsed diode laser (LDH-P-C-405, PicoQuant) operated at 40 MHz with a defined 'start', and 'stop' signal methodology which allows for the arrival of multiple (burst) of photons to the sample and the measurement of the phosphorescence decay occurring after a defined start-stop delay. The measurement is repeated many times in order to build a histogram of the phosphorescence decay during the acquisition of the PLIM image. with an optical power between 0.3-0.8 μW.

The emitted fluorescence is spectrally cleaned with a dichroic mirror and a transmission band edge filter (488 nm). A pinhole of 75 μm or 150 μm is employed to reject light that is out of focus. The fluorescence is detected using single photon counting with an avalanche diode (SPAD-100, PicoQuant) and digitised with a Time Harp 260 PCI card (PicoQuant).

Image scans are performed over an area of 80 × 80 μm^2 with a varied pixel composition ranging from 256 × 256 pixels up to 640 × 640 pixels. The overall number of photons per image was used as the measured decay curve. Lifetime image analysis was not suitable with the samples because of low photon counts detected per pixel but PLIM analysis was possible for the deposited-on glass because of higher photon count rates. All decay curves were analysed using multi-exponential models using the SymPhoTime software (PicoQuant). Fit quality was assessed from the χ^2 parameter and weighted residuals. Examples of FLIM images from ReC16 monolayer deposited on c-Si substrates at different distances to the silicon surface and the overall phosphorescence decay curve is shown in Fig. S7. Also shown is the PLIM images and overall decays for a 5L ReC16 LB film deposited on a fused silica substrate and the effect of the SA capping layer on the measured lifetime.

The PLIM images show a highly ordered honeycomb-like structure assigned to the Re moiety. While the SA units are of high symmetry in this plane and able to pack closely without imposing any further structure on the system, the cationic rhenium complex head groups and the tetrafluoroborate anions will require a packing arrangement that separates ions of like charge while maximising attractive forces such as dipole−dipole interactions and van der Waals forces. We were unable to obtain a single crystal structure of the ReC16 complex to provide suggestions as to the nature of the stacking, but the closest analogue to have been characterised by single crystal diffraction,[1] in which the C16 chain is replaced by a cyclohexyl group, shows a zig−zag arrangement of rhenium cations and tetrafluoroborate anions that on the macroscale form linear chains of what in the present system constitute the polar head groups. It is suggested that the honeycomb structure of the ReC16 monolayers results from the expected stacking of the C16 chains away from the interface, with the additional formation of linear chains of closely packed anion-cation aggregates in the orthogonal plane, which interweave to form a network as observed in Fig. S7

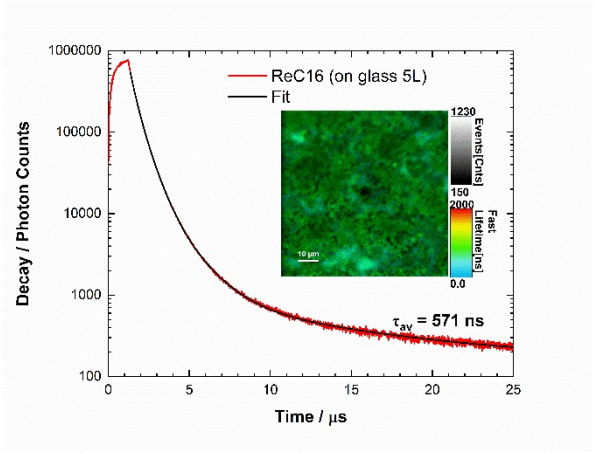

(a)

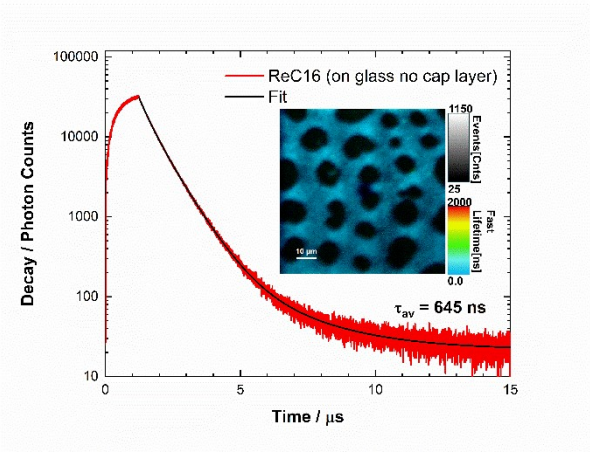

(b)

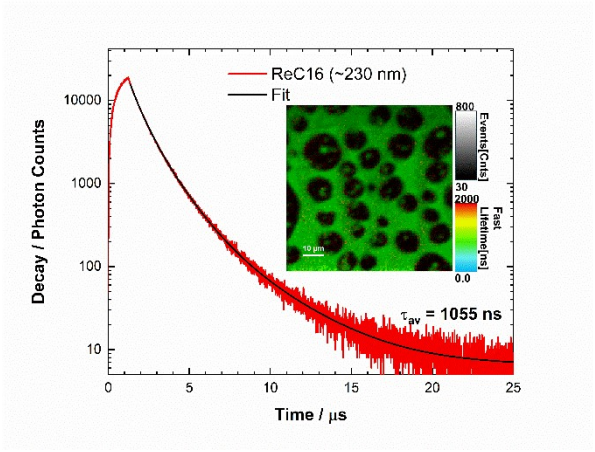

(c)

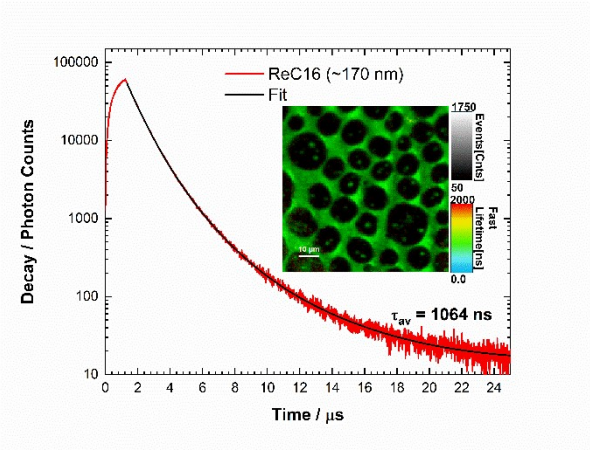

(d)

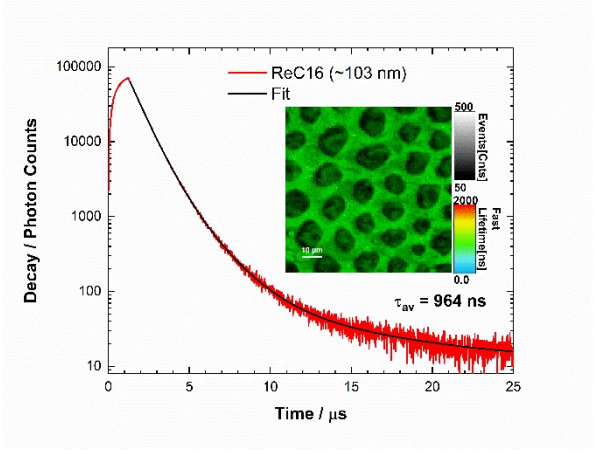

(e)

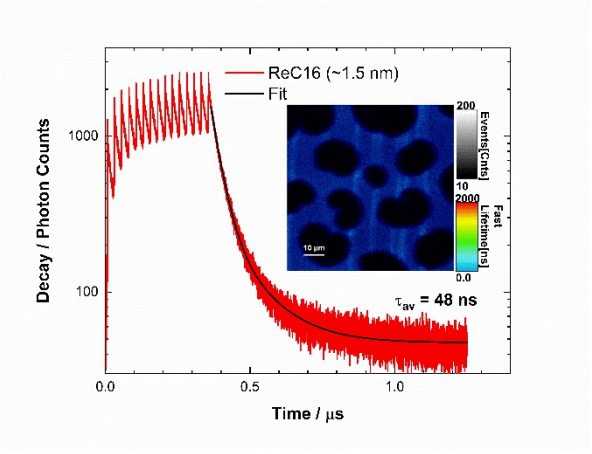

(f)

Fig. S7 Examples of PLIM and corresponding decay curves from a ReC16 monolayer on glass and silicon substrates observed at different distances to the surface.

7. Analysis of time resolved phosphorescence decays

The phosphorescence decay intensities were analysed using a multi-exponential model as the sum of single exponential decay curves:[4]

$$I(t) = \sum_{i=1}^{n} A_i \cdot e^{\left(-\frac{t}{\tau_i}\right)} \qquad \text{(Eq. S1)}$$

where τ_i are the decay lifetimes with amplitudes A_i of the components at $t = 0$ and n is the number of decay lifetimes.

The fractional contribution (f_i) of each decay component to the steady state intensity is given by

$$f_i = \frac{A_i \cdot \tau_i}{\sum_j A_j \cdot \tau_j} \qquad \text{(Eq. S2)}$$

The average lifetimes can be defined in two ways, and they differ in the way the decay lifetimes are weighted in the averaging:

$$\tau_{AV1} = \frac{\sum_i A_i \cdot \tau_i^2}{\sum_i A_i \cdot \tau_i} \qquad \text{(Eq. S3)}$$

τ_{AV1} equals the average amount of time the fluorophore remains in the excited state after the start of the excitation:

$$\tau_{AV2} = \frac{\sum_i A_i \cdot \tau_i}{\sum_i A_i} \qquad \text{(Eq. S4)}$$

τ_{AV2} is proportional to the area under the decay curve and is mainly used in lifetime based Förster resonance energy transfer (FRET) efficiency estimation.[3]

$$E = 1 - \frac{F_{DA}}{F_D} = 1 - \frac{\int I_{DA}(t)dt}{\int I_D(t)dt} \qquad \text{(Eq. S5)}$$

where $I_{DA}(t)$ and $I_D(t)$ are the intensity decays of the donor in the presence and absence of the acceptor energy transfer respectively. The integrals are proportional to the steady state fluorescence intensities in the presence (F_{DA}) and absence (F_D) of the acceptor energy transfer. All lifetimes fitted in this work for the ReC16 monolayers have used the τ_{AV2} averaged lifetime fitted with a two or three exponential model.

8. Spectroscopic ellipsometry measurements

The thickness of the deposited LB layers and the oxides were measured initially with single wavelength ellipsometry (Rudolph AutoEL III) at 70° incidence angle equipped with a He-Ne laser wavelength of 632.8 nm. A simple oxide model was used for the estimate the overall thickness of the LB layers and oxides on silicon. Five or six measurements were taken from each sample and averaged out. The estimated standard error was in the range of 0.1%-1%. The measurements were repeated and confirmed with spectroscopic ellipsometry from 400 nm to 700 nm at an incidence angle of 70° using a spectroscopic phase modulated ellipsometer (Uvisel from Horiba Jobin-Yvon) with a Xe arc illuminator fibre optic. For the LB films, a three-layer model (substrate/monolayer/air) using silicon for the substrate and a Cauchy model for the stearic acid monolayers[5] was employed for the analysis of the data within the DeltaPsi2 software. Three readings were taken from each sample and averaged out. The errors were less than 1%. Examples of model fits are shown in Fig. S8 and the estimation of the film thicknesses.

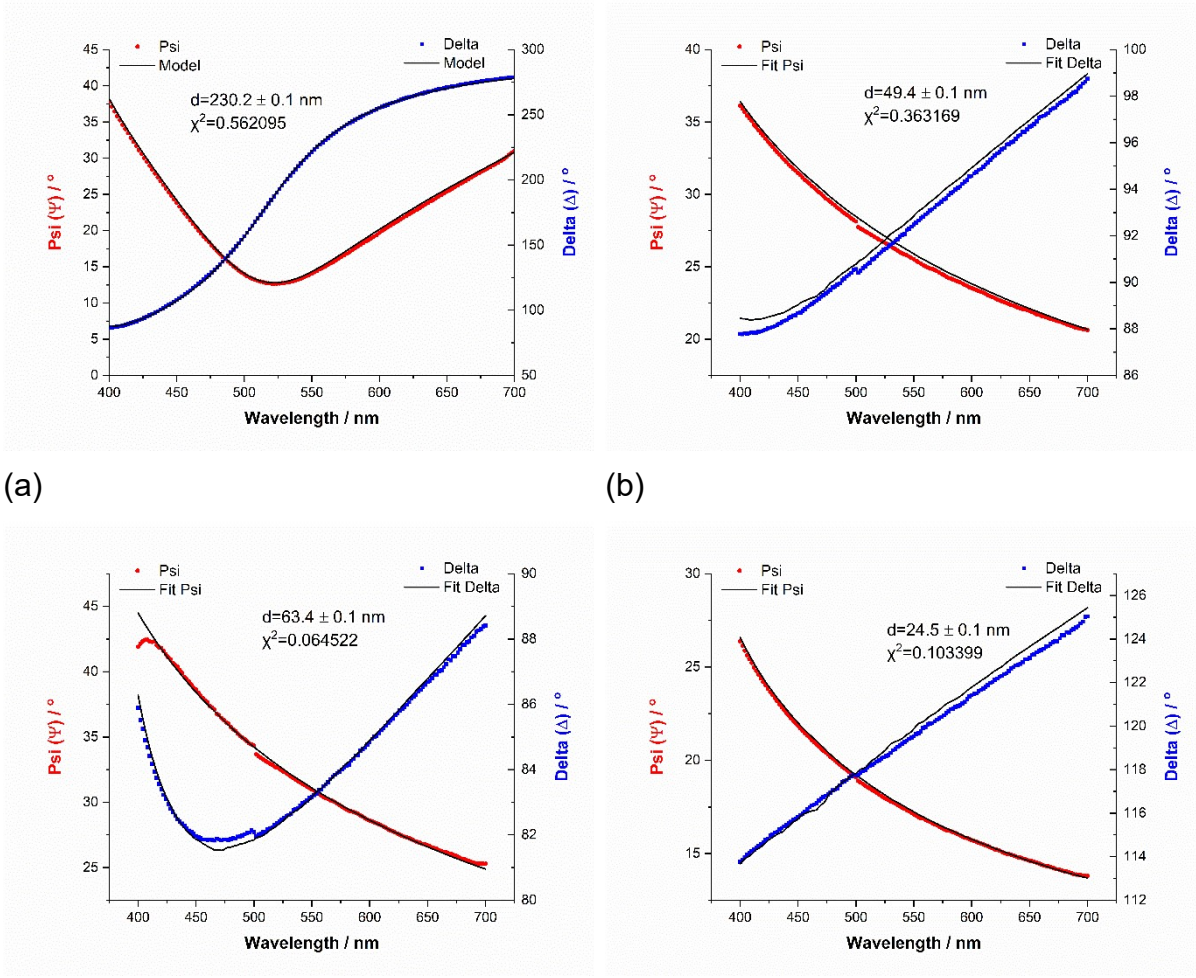

Fig. S8 Examples of ellipsometry measurements and model fit using spectroscopic ellipsometry for various thickness thermal oxide (a) and stearic acid (b, c and d) film thicknesses. The estimated film thickness and standard error is shown for each

measurement.

9. Modelling using the CPS model

A classical model developed by Chance, Prock and Silbey (CPS) to model molecular fluorescence near an interface was modified and used for silicon surfaces.[6] The excited ReC16 molecules were modelled as forced damped electric dipole oscillators and the complex dielectric constant of silicon at the maximum emission wavelength of ReC16 (λ=535 nm) was used for the modelling of the equations. The equations and details of our approach can be found in previous work.[7]

Fig. S9 shows the model fit to the experimental results for different ReC16 transition dipole orientations, where P and S correspond to vertical emission transition dipole moment (0°) and horizontal emission transition dipole moment (90°) respectively. The lifetime error bars were estimated from multiple samples (at least two) and from repeated measurements on the same sample but on different spot (at least three).

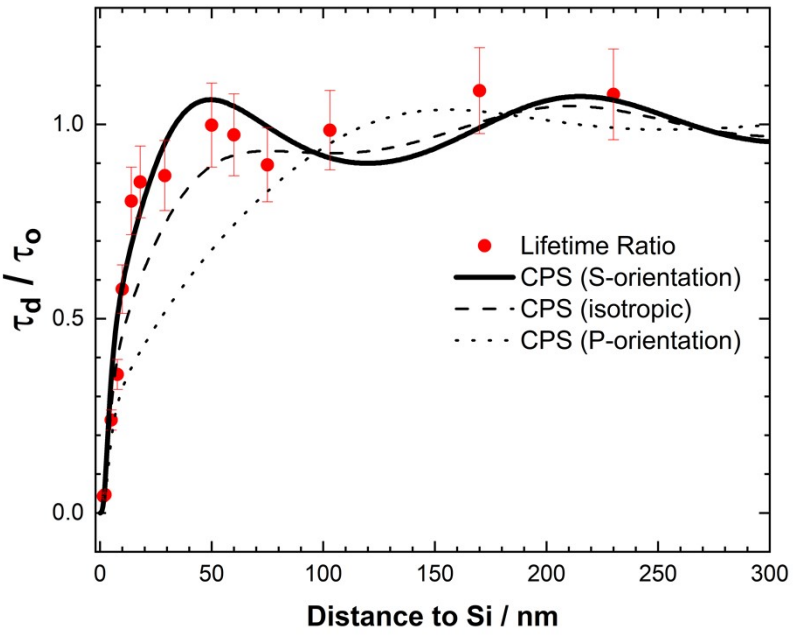

Fig. S9 CPS model for three different transition dipole orientations of the ReC16 emitter chromophore with respect to the surface of silicon with a QY=75%. The measured experimental lifetimes are shown together with the model lines. Error bars are ±10%.

A simple kinetic model can be used to show that the appropriate quantum yield to use in the CPS model is the quantum yield for transitions originating from the triplet state (as also used by CPS themselves)[6] rather that the (much smaller) quantum yield for optical emission.

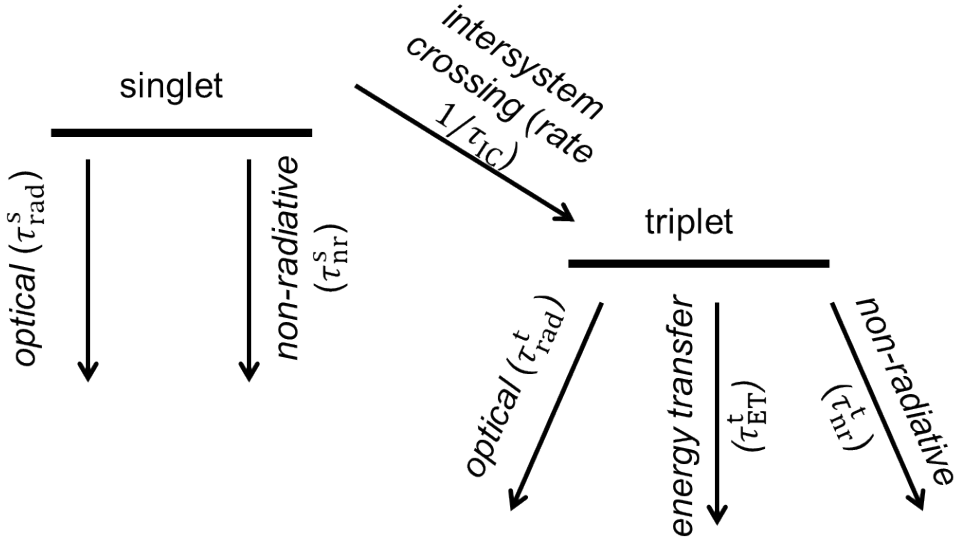

Fig. S10 Schematic of a simple energy level model for the excitation of ReC16 near the surface of silicon and associated lifetimes.

Neglecting emission from the singlet and the back transfer from the triplet to singlet, the kinetics of the singlet (n_s) and triplet (n_t) populations is governed by (see Fig. S10 for definition of lifetimes)

$$\frac{dn_s}{dt} = -\frac{n_s}{\tau_{nr}^s} - \frac{n_s}{\tau_{IC}} = -\frac{n_s}{\tau^s} \qquad \text{(Eq. S6)}$$

$$\frac{dn_t}{dt} = \frac{n_s}{\tau_{IC}} - \frac{n_t}{\tau^t} \qquad \text{(Eq. S7)}$$

where

$$\frac{1}{\tau^s} = \frac{1}{\tau_{nr}^s} + \frac{1}{\tau_{IC}} \quad \text{and} \quad \frac{1}{\tau^t} = \frac{1}{\tau_{rad}^t} + \frac{1}{\tau_{ET}^t} + \frac{1}{\tau_{nr}^t}$$

are the total decay rates of the singlet and triplet states. The solution of Eqs. (S6), (S7) with the initial condition $n_s = 1$, $n_t = 0$ is

$$n_s(t) = e^{-t/\tau^s} \qquad \text{(Eq. S8)}$$

$$n_t(t) = \frac{1}{\tau_{IC}\tau^t - \tau^s}\left(e^{-t/\tau^t} - e^{-t/\tau^s}\right)q^{s-t}e^{-t/\tau^t} \quad \text{(Eq. S9)}$$

where, in the third equation (S8), we neglected the second exponential in (S9) (describing the population rise in the triplet state) and introduced the ratio $q^{s-t} = \tau^s/\tau_{IC}$. This ratio (which can be called the yield of transfer to the triplet) is small, and is the reason for the small yield of optical emission from the triplet. The third, approximate, equation (S9) is accurate since $\tau^t \gg \tau^s$ on account of the fast rate of intersystem crossing. The small yield q^{s-t} is equal to the population of the triplet state very soon – in effect, immediately - after the initial excitation of the singlet state.

The observed rate of energy transfer from the triplet state is then

$$\left(\frac{dn_t}{dt}\right)_{Energy\ Transfer} = \frac{n_t\, q^{s-t}}{\tau_{ET}^{\,t}\,\tau_{ET}^{\,t}}e^{-t/\tau^t} \quad \text{(Eq. S10)}$$

The rate of energy transfer $1/\tau_{ET}^{\,t}$ which corresponds to *b* (Eq. 2.39 & 2.40) in CPS theory[6] is therefore multiplied by q^{s-t} as a result of the small occupation of the triplet state. Similarly, the observed decay rate at large separation from the absorber when there is no energy transfer, is given by

$$\left(\frac{dn_t}{dt}\right)_{large\ seperation} = \frac{n_t}{\tau_{rad}^{\,t}} + \frac{n_t}{\tau_{nr}^{\,t}} = \frac{q^{s-t}}{q\tau_{rad}^{\,t}}e^{-t/\tau^t} \quad \text{(Eq. S11)}$$

where

$$q = \frac{\tau_{nr}^{\,t}}{\tau_{nr}^{\,t} + \tau_{rad}^{\,t}} \quad \text{(Eq. S12)}$$

It is the yield q of transitions from the triplet state, given by (S12), that divides the radiative rate $1/\tau_{rad}^{\,t}$. This parallels the quantity q that divides the radiative rate b_r in the CPS theory (equation 2.41)[6]. The ***observed*** decay rate at large separation, on the other hand, is again multiplied by the small number q^{s-t}. CPS theory normalises the energy transfer rate *b* by the decay rate b_r/q. The corresponding

ratio of the ***observed*** two rates, given by the ratio of the pre-exponential factors in (S10) and (S11), therefore also contains only the yield *q* as the yield of transfer to the triplet q^{s-t} cancels out.

Similar best-fit QY observations have also been observed for a series of different quantum dots deposited on silicon substrates which gave good agreement with similar model with high quantum yields.[8] Different CPS model curves are shown in Fig. S11 for different QY values. The QY was the only parameter in the CPS model fit. We have chosen a best fit by minimising the sum of the error in the lifetime data and the model fit, Sum[$(data_i\text{-}model_i)^2$]. The minimum sum or errors is given with an estimated QY is 85%. There is a plateau for values of the QY between 65%-100%. See also Figure S12.

In order to demonstrate unequivocally that the energy transfer from the metal complex, ReC16, monolayer leads to electron-hole generation in c-Si wafer substrates additional experiments are required such as silicon photoluminescence (excitation spectrum) or photocurrent measurements. However, such measurements are hampered by the weak absorption of the metal complex monolayer against the background of strong silicon absorption: at the wavelength of 375nm, the monolayer absorbs 0.2% of the incident light against virtually 100% by silicon in any thickness over 0.5 µm.

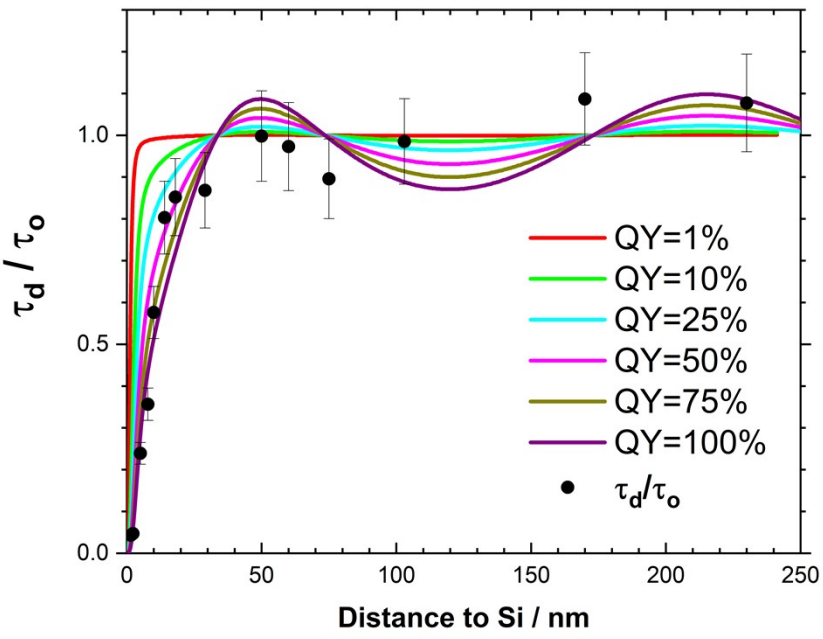

Fig. S11 CPS model for S orientation for different QY of the ReC16 monolayer. The measured experimental lifetimes are shown together with the model lines. Error bars are 10%.

(a) (b)

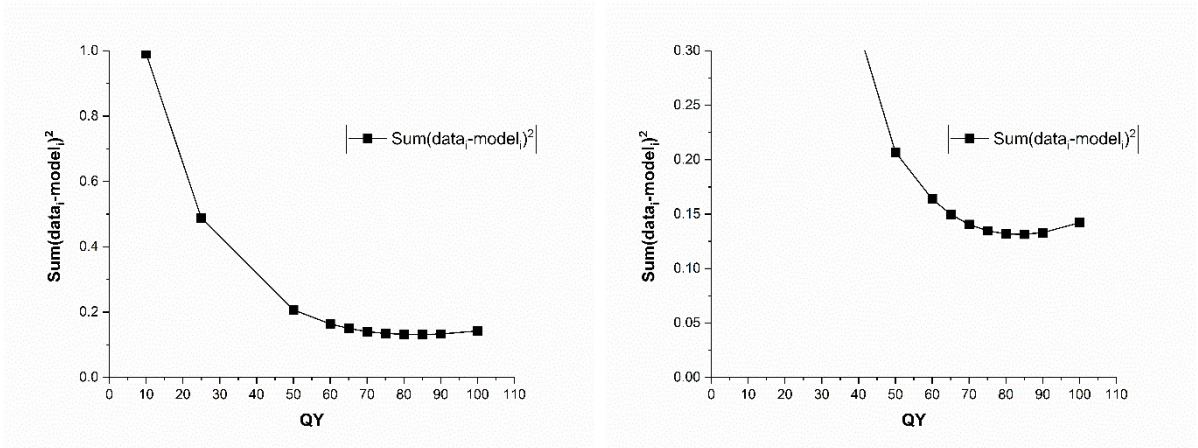

Fig. S12 Estimation of the minimum for the Sum[(data$_i$-model$_i$)^2] for various assumed QY in the CPS model. (a) full data and (b) shows the plateau observed as a function of QY for values above 65%.

10. References

1 V. Fernández-Moreira, F. L. Thorp-Greenwood, A. J. Amoroso, J. Cable, J. B. Court, V. Gray, A. J. Hayes, R. L. Jenkins, B. M. Kariuki, D. Lloyd, C. O. Millet, C. F. Williams and M. P. Coogan, *Org. Biomol. Chem.*, 2010, **8**, 3888.

2 A. M. Borys, *Organometallics*, 2023, **42**, 182–196.

3 J. R. Lakowicz, *Principles of fluorecence spectroscopy*, Springer US, New Jersey, Third., 2006.

4 K. Ray, R. Badugu and J. R. Lakowicz, *Langmuir*, 2006, **22**, 8374–8378.

5 G. Gonella, O. Cavalleri, I. Emilianov, L. Mattera, M. Canepa and R. Rolandi, *Mater. Sci. Eng. C*, 2002, **22**, 359–366.

6 R. R. Chance, A. Prock and R. Silbey, in *Advance in Chemical Physics*, 1978, vol. XXXVII, pp. 1–64.

7 L. Danos, N. R. Halcovitch, B. Wood, H. Banks, M. P. Coogan, N. Alderman, L. Fang, B. Dzurnak and T. Markvart, *Faraday Discuss.*, 2020, **222**, 405–423.

8 M. T. Nimmo, L. M. Caillard, W. De Benedetti, H. M. Nguyen, O. Seitz, Y. N. Gartstein, Y. J. Chabal and A. V. Malko, *ACS Nano*, 2013, **7**, 3236–3245.